# Mapping Crustal and Uppermost Mantle Deformation in the Westernmost Mediterranean by Radial Anisotropy

**Lili Feng**

Department of Physics, University of Colorado Boulder, Boulder, CO 80309, USA

Corresponding author: Lili Feng (lili.feng@colorado.edu)

**Keywords:**

- Westernmost Mediterranean
- Joint inversion
- Radial anisotropy
- Cenozoic extension
- Africa-Iberia movement
- Mantle flow

**Abstract**

The Mediterranean is a unique place for geoscientists to investigate driving tectonic forces within a complex mobile belt. The tectonic and geodynamical history of the eastern and middle Mediterranean region since the late Eocene is relatively well documented (Faccenna et al., 2014), however, tectonic evolution of the westernmost Mediterranean remains debated. The relative movement between the African plate and the Iberian microplate during the Cenozoic is key to improved understanding of the tectonics of the westernmost Mediterranean. Using seismic data from 1186 stations deployed across the westernmost Mediterranean, I construct a 3-D radially anisotropic model from a joint inversion of Rayleigh and Love wave dispersions, along with receiver functions. The new model provides several tectonic implications. (1) The crustal radial anisotropy identifies regions that have undergone extension from the early Oligocene to the lower Miocene, providing seismic evidence for a better understanding of the Africa-Iberia movement during the Cenozoic Era. (2) Strong crustal radial anisotropy beneath the Betic Mountains could be physically related to the extensional collapse process. (3) Inferred mantle anisotropy identifies regions with strong anisotropy which are predicted by geodynamical modelling. The mantle anisotropy map could potentially lead to a better understanding of the present-day mantle flow pattern on regional scale.

# 1. Introduction

## 1.1 Tectonic Background

Sitting between the Eurasian and the Africa plate, the Mediterranean region has experienced a complex tectonic evolution marked by oceanic lithosphere subduction and associated crustal and mantle deformational processes. The region presents a variety of tectonic features and events, including arcuate belts, sedimentary basins, mountain edifices, active volcanoes and large earthquakes. The tectonic and geodynamical history of the eastern and middle Mediterranean region for the past ~ 35 Ma is relatively well investigated, as summarized by Faccenna et al. (2014). However, formation of several tectonic features in the western Mediterranean (**Fig. 1b**) is still under debate. For example, the development of the Betic-Rif mountain belt could be explained by several hypotheses, including delamination or rolling back of the slab (e.g., Lonergan & White, 1997; Faccenna et al., 2004; Spakman & Wortel, 2004), change in subduction polarity (Vergés & Fernàndez, 2012) and extensional collapse (Platt et al., 1989; Molnar & Houseman, 2004). And the boundary of the westward extension of the Alboran region is estimated differently (e.g., Lonergan & White, 1997; Faccenna et al., 2004; Spakman & Wortel, 2004). Key to an improved understanding of the tectonic evolution of the western Mediterranean is the reconstruction of the relative movement between the African plate and the Iberian microplate since the Cenozoic (De Vincente & Vegas, 2009). The Africa-Iberia movement has dominantly controlled the evolution of the Mediterranean basins and formation of several mountain ranges, including the Pyrenees, the Iberian Chains, the Betic-Rif Belt and the Atlas Mountains (Di Bucci et al., 2010; Laville et al., 2004; van Hinsbergen et al., 2014).

## 1.2 Previous tomographic studies

Seismic tomographic models are crucial for better understanding of the tectonics of the western Mediterranean. Earliest regional models covering the region can date back to 1970s presented by Nolet (1977), in which the author used Rayleigh waves from a few seismic stations to infer upper mantle structure. More recent seismic studies imaging the crustal and mantle structure beneath the Mediterranean has been based on different approaches, including receiver functions (e.g., de Lis Mancilla & Diaz, 2015), surface wave tomography (e.g., Palomeras et al., 2017), body wave tomography (e.g, Bonnin et al., 2014) and full-waveform inversion (FWI) (e.g., Zhu & Tromp, 2013; Fichtner & Villaseñor, 2015). Most of the existing tomographic studies focuses on determination of isotropic structures, with a few exceptions. For instance, based on seismic data from 278 stations, Fichtner & Villaseñor (2015) determined Vsv/Vsh structures of the western Mediterranean using full-waveform inversion based on regional and local earthquake data. However, because the authors only used earthquake waveforms, which has lower signal-to-noise ratio at higher frequencies compared with ambient noise interferograms, the resolution of crustal anisotropy presented by Fichtner & Villaseñor (2015) may not be optimal. Indeed, as admitted by the authors, the inferred crustal anisotropy in Fichtner & Villaseñor (2015) may be strongly biased by event mislocation and near-field affect, producing artefacts of negative anisotropy associated with earthquake locations.

### 1.3 This study

In this study, I present a new 3-D radially anisotropic model of the crust and uppermost mantle beneath the westernmost Mediterranean, including southmost of France, the Iberian Peninsula and northern Morocco. The model is constructed by a Bayesian Monte Carlo joint inversion of Rayleigh and Love wave dispersion data and receiver functions, with dispersion measurements extracted from both ambient noise and earthquake waveforms. This study uses a large seismic dataset from 1186 seismic stations deployed in and surrounding the westernmost Mediterranean (**Fig. 1**), including the IberArray (IB), the PYROPE array (X7), the PICASSO array (XB) and some other networks.

The Vsv structures resolved by the model are generally consistent with previous tomographic studies (e.g., Fichtner & Villaseñor, 2015; Palomeras et al., 2017). Besides, the newly inferred crustal anisotropy identifies regions may have undergone Cenozoic extension, providing seismic evidence for a better understanding of the relative Africa-Iberia movement during the Cenozoic Era. Uppermost mantle anisotropy presented in this study can also be useful as an indicator to infer present-day mantle flow pattern.

## 2. Data and Methodology

### 2.1 Seismic Station Distribution

This study utilizes a seismic dataset including 48 permanent and temporary networks distributed within a distance of ~ 1500 km from the center of the Iberian Peninsula between January 2007 and April 2014 (**Fig. 1a**). The dataset includes 1186 broadband seismic stations in total, which is the most complete datasets ever used for seismic tomography across the westernmost Mediterranean. The most important three networks are the IberArray (IB) deployed across the Iberian Peninsula, the PYROPE array (X7) covering the Pyrenees and surroundings, and the PICASSO array (XB) distributed at southern Spain and Morocco. Those three networks include 459 stations and they are identified with blue, red and green colors in **Figure 1.** Other networks are colored in yellow. **Table S1** summarizes all the seismic networks and associated DOI.

## 2.2 Ambient Noise Tomography

### 2.2.1 Two-station interferometry

Continuous seismic waveforms are routinely processed with the two-station ambient noise interferometry method, namely, noise correlation (Bensen et al., 2007; Ritzwoller & Feng, 2019) to construct two-station interferograms which include surface wave arrivals. Rayleigh wave dispersions can be extracted from the vertical-vertical (ZZ) component interferograms and Love wave phase arrivals are retrieved from the transverse- transverse (TT) component.

### 2.2.2 Three-station direct wave interferometry

To further enhance surface wave data coverage at short periods, so that the crustal structures can be better resolved, a recently developed three-station direct wave interferometry technique is applied (Zhang et al., 2020). Both the ZZ and TT component two-station interferograms are used to construct the three-station interferograms as supplementary datasets to improve path coverage. The three-station interferometry workflow is directly taken from Feng (2021), which is slightly different from Zhang et al. (2020)'s approach.

Previous studies of three-station direct wave interferometry only applied the technique to ZZ component interferograms (Feng, 2021; Zhang et al., 2020), this study extends the usage of the three-station method to TT components so that Love wave data coverage can also be improved, resulting in more reliable determination of crustal radial anisotropy.

Incorporating three-station interferograms as additional dataset for surface wave tomography has two advantages. (1) Asynchronous interferograms between stations that are not deployed simultaneously could be constructed. **Figure 2a and 2b** show a subset of the ZZ and TT component asynchronous interferograms, with SNR larger than 15 (ZZ) or 10 (TT). For those asynchronous interferograms, at least one station belongs to the IB, XB or X7 networks. As marked on the figures, the three-station interferograms provide > 62,000 additional paths for Rayleigh waves linking the IB, XB, or X7 stations with other networks, and > 38,000 additional paths for Love waves. (2) Three-station interferograms typically yield surface wave phase arrivals with higher SNR ratio, as demonstrated by Feng (2021) and Zhang et al. (2020) and also illustrated by the sample interferograms in **Figure 2c and 2d**.

Automatic frequency-time analysis (FTAN) is applied to both two- and three-station interferograms to measure the dispersive arrivals of surface waves, yielding Rayleigh wave dispersion curves of periods 8 – 50 s and Love wave measurements of 8 – 40 s. Then I apply the eikonal tomography (Lin et al., 2009) to determine 2-D phase speed maps for Rayleigh and Love waves.

### 2.3 Earthquake Tomography

Eikonal tomography is also applied to dispersion measurements extracted from teleseismic earthquake waveforms (ISC catalog, 2007 – 2014, $M_s$ > 5.5), for both Rayleigh and Love waves at periods of 26 s – 50 s. Above 50 s period (Rayleigh wave only), Helmholtz tomography is performed to take into account finite frequency effect (Lin & Ritzwoller, 2011). Rayleigh wave earthquake phase speed maps are produced at periods of 26 s – 85 s, while Love wave maps do not extend to periods longer than 50 s. The final phase velocity maps are constructed by combining ambient noise and earthquake results.

### 2.4 Receiver Function Analysis

In order to better determine crustal thickness, receiver functions are computed in this study. An iterative deconvolution algorithm (Ligorria & Ammon, 1999) is applied to teleseismic P wave arrivals from earthquakes with $M_w$>5.5 and epicentral distances between 30°- 120°, producing radial component P-wave receiver functions. Then a harmonic stripping approach (Shen et al., 2012) is applied to remove the impact of azimuthal anisotropy and dipping interface, resulting in the isotropic component of P-wave receiver function. The isotropic P-wave receiver function is the final product of receiver function analysis to be used for the joint inversion.

## 3. Rayleigh and Love wave phase speed maps

In **Figure 3**, I present sample phase speed maps for both Rayleigh and Love waves. Several geological structures can be identified at different periods and here I list a few notable examples.

(1) The Iberian Massif emerges as a large-scale high-velocity block at shorter periods (T = 10 and 20 s) for both Rayleigh and Love waves.

(2) The locations of the Alentejo-Guadalquivir Basin, the Rabat Basin and the Rif Basin are captured with extremely low speed at all the periods except T = 70 s Rayleigh wave map. The low-speed anomaly at those locations reflects slow Vsv/Vsh structure in the sediments at shorter periods (T < ~20 s), while the low velocity at intermediate periods (T = 30 – 50 s) infers thick crust.

(3) The Pyrenees is identified with relatively high speed at T = 10 s Rayleigh wave map, while it becomes a low velocity stripe in the T = 30 s Rayleigh wave map.

(4) The Iberic Chain and surroundings are imaged with relatively low speed in the T = 20 s and 30 s period Rayleigh wave map.

(5) At longer periods (> 40 s), Rayleigh wave maps identify slow speed anomaly at the Atlas Mountains.

(6) There is a sharp velocity contrast near the Toulouse Fault in longer periods (> 40 s) Rayleigh wave speed maps.

(7) At 70 s period, high-speed anomaly near the Alboran Sea is resolved in the Rayleigh wave map.

Rayleigh and Love wave phase speed maps, along with receiver functions, are the input for the Bayesian Monte Carlo inversion to infer shear wave velocity structure with radial anisotropy.

## 4. Bayesian Monte Carlo Inversion

A Bayesian Monte Carlo inversion is performed to construct a 3-D anisotropic Vs model, on a regular geographical grid with spacing of ~ 20 km (0.2° by longitude and latitude). Input for the Bayesian inversion includes local Rayleigh and Love wave dispersion curves taken from phase speed maps, along with receiver functions. The inversion workflow is taken from Shen et al. (2012), Feng & Ritzwoller (2019) and Feng (2021), which naturally takes into account the reference model and additional prior constraints. In the following subsections, I briefly summarize the model parameterization, reference model, prior constraints, Monte Carlo sampling procedure, and finally, construction of a final 3-D model. More technical details can be found in Feng & Ritzwoller (2019) and Feng (2021).

### 4.1 Model parametrization and perturbation ranges

At each inversion grid point, a radially anisotropic Vs profile (0-200 km) is fully described by 15 model parameters. The allowed perturbation ranges for each parameter are defined based on the reference model (CRUST-1.0 and ak135 model).

1. Sedimentary layer (Vsv), 3 parameters: Three parameters are used to determine sedimentary structure, including Vsv at the top and bottom of the sediments along with sedimentary thickness. Vsv at intermediate depth inside the sedimentary basins increase linearly with depth. Vsv values can vary from 0.2 km/s to 2.5 km/s and the sedimentary thickness is allowed to perturb from 0 to twice of the reference value. The reference thickness is taken from the CRUST-1.0 model (Laske et al., 2013).
2. Crystalline crust (Vsv), 5 parameters: Vsv inside the crystalline crust is defined by four cubic B-splines. The corresponding B-spline coefficients are model parameters to be determined from the inversion. In addition, crustal thickness is another model parameter that needs to be inferred. The Vsv values in the crystalline crust are allowed to vary $\pm 20\%$ with respect to the reference values taken from the 1-D ak135 model (Kennett et al., 1995). The perturbation range of crustal thickness depends on the reference value $m_0$ taken from the CRUST-1.0 model (Laske et al., 2013): (1) If $m_0$ > 20 km, the thickness varies by $\pm$ 50% around $m_0$; (2) If 10 km $\leq m_0 \leq$ 20 km, the thickness can perturb by $\pm$ 10 km; (3) If $m_0 \leq$ 10 km, the thickness perturbs from 0 to twice of the reference value.
3. Mantle (Vsv), 5 parameters: Mantle Vsv structure is determined by five cubic B-splines. Therefore, five B-spline coefficients need to be inferred by the inversion.
4. Radial anisotropy ($\gamma$), 2 parameters: The shear wave radial anisotropy, is the difference in propagation wave velocity between horizontally (Vsh) and vertically (Vsv) polarized shear waves. The strength of the radial anisotropy, $\gamma$, is defined as

$$\gamma = \frac{(V_{sh} - V_{sv})}{V_s} \tag{1}$$

where $V_s = (V_{sh} + V_{sv})/2$. Similar to Feng & Ritzwoller (2019), I use a simple parameterization for radial anisotropy. Namely, the radial anisotropy is assumed to be vertically uniform in the crystalline crust and mantle respectively. The strength of crustal ($\gamma_c$) and mantle ($\gamma_m$) radial anisotropy are allowed to perturbed $\pm$ 10%. As shown by **Figure 8b**, such a simple two-layer anisotropic model suffices to fit data at most places.

The laminated structure in the sedimentary basins could produce significantly large radial anisotropy, which could bias the estimation of radial anisotropy in the crystalline crust, as discussed by Feng & Ritzwoller (2019). However, most locations across the study region have relatively thin sedimentary layer (< 3 km) and thus the impact from sedimentary basin on dispersion data is negligible.

**Table S2** summarizes the range of each model parameter.

### 4.2 Additional prior constraints

To exclude physically unrealistic models, additional prior constraints are implemented in the inversion process (Feng & Ritzwoller, 2019), including: (1) Velocity jumps in both Vsv and Vsh are positive at each Earth's interface. (2) Vsv and Vsh are constrained to be less than 4.3 km throughout the crust. (3) In the crust, Vsv and Vsh monotonically increase with depth. (4) Vsv and Vsh are constrained to be in the range of 4.0 km/s ~ 4.6 km/s at the shallowest layer in the mantle. (5) Vsv and Vsh are not allowed to exceed 4.9 km/s at all depth ranges. (6) Vsv and Vsh are larger than 4.3 km/s at 200 km depth (bottom of the model). (7) To discourage spurious vertical oscillations in the mantle, the difference at the local maxima and minima in Vsv and Vsh cannot exceed 10 m/s.

The additional prior constraints help excluding nonphysical models, and they also have an impact on the prior distribution. Indeed, as shown in **Figure 4**, the prior distributions of crustal thickness and Vsv are non-uniform due to the model parameterization and additional prior constraints.

### 4.3 Posterior Distributions

Posterior distributions of the model parameters are produced from the Markov Chain Monte Carlo (MCMC) sampling process based on data fitness. A model is accepted to construct the posterior distribution if its corresponding data misfit is smaller than $\chi_{min} + 0.5$, where $\chi_{min}$ is the misfit value of the model the best fitting the Rayleigh and Love wave dispersion, along with receiver function. Details about the MCMC sampling process can be found in Shen et al. (2012), Feng & Ritzwoller (2019) and Feng (2021). Example posterior marginal distributions of Vsv at 15 and 80 km depths, along with crustal thickness, are presented in **Figure 4**.

### 4.4 Constructing 3-D model

At each station inside the study region, a Bayesian Monte Carlo inversion is performed based on Rayleigh and Love wave phase speed curves along with receiver functions. However, as shown in **Figure 3**, both Rayleigh and Love wave phase speed maps extend to offshore region where receiver functions are not available. To make the final 3-D model cover the offshore area, I perform another group of inversion on a regular geographical grid with spacing of ~ 20 km (0.2° by longitude and latitude), using surface wave dispersion data only. Then, using Shen et al. (2018)'s and Feng (2021)'s approach, a final radially anisotropic Vs model is obtained by merging the station-based model with the grid-point based model.

## 5. Results

The output of the Bayesian Monte Carlo inversion is a 3-D shear wave velocity model with radial anisotropy, extending to a maximum depth of 200 km.

### 5.1 Crustal Vsv

**Figure 5a, 5b and 5c** present Vsv slices in the crust, at three sample depths of 3 km, 10 km and 20 km (central-depth $\pm$ 3 $km$). The locations of major sedimentary basins are captured in the 3 km slice, including the Aquitaine Basin located north to the Pyrenees; the Alentejo-Guadalquivir Basin covering the Gulf of Cadiz; the Rabat Basin west to the Rif mountains; and the Rif Basin located at Rif but also extends offshore to the Alboran Sea (Pawlewicz et al., 1997). The Iberian Massif emerges as a relatively high-speed anomaly at 3 km depth and its boundary is well captured by the model. At 10 km depth, both the Pyrenees and the Iberian Chain are imaged as relatively high-velocity stripes, and the high-speed anomaly representing the Iberian Massif becomes more prominent. The Betic-Rif Belt and surroundings emerge with extremely slow Vsv. Going deeper to 20 km depth, the Pyrenees high-speed stripe disappears while the Iberian Chain stripe, the Iberian Massif and the Betic-Rif Belt anomaly can still be identified. Extremely high Vsv beneath Alboran Sea emerges, indicating shallow Moho at this location.

### 5.2 Crustal Thickness

**Figure 6b** is a crustal thickness map constructed in this study. Not surprisingly, the map identifies relatively thick crust at Pyrenees, the Iberian Chain, the Betic-Rif Belt and the Atlas Mountains. In contrast, very thin crust is resolved beneath the Alboran Sea and the Bay of Biscay. **Figure 6a** presents the CRUST-1.0 model for comparison. The crustal thickness map from this study has much higher resolution and the CRUST-1.0 model fails to identify thick crust at the Iberian Chain and the Betic-Rif Belt.

### 5.3 Mantle Vsv

To illustrate Vsv distribution in the mantle, three sample Vsv slices at 60 km, 80 km and 100 km depths (central-depth $\pm$ 3 $km$) are presented as **Fig. 5d, 5e and 5f**. The Massif Central, located at the northeastern corner of the map, is resolved as a low-Vsv anomaly whose western boundary is defined by the Toulouse Fault. West to the Toulouse Fault, the Eurasian continental lithosphere emerges with extremely high Vsv, probably indicating a rigid lithospheric domain. At 60 km depth, the central part of the Pyrenees has relatively low Vsv than its surroundings, while the slightly low-Vsv region changes its distribution at 80 km and 100 km depths. The Iberian Massif emerges with a variant distribution of Vsv in the 60 km map, however, moving deeper to 100 km depth, the Iberian Massif is resolved with low Vsv. High Vsv is imaged beneath the Betic-Rif Belt at all depth slices in the mantle. In Morocco, a relatively uniform low-speed block emerges beneath the Atlas Mountains and surroundings, probably indicates thin lithosphere.

### 5.4 Radial Anisotropy

Crustal ($\gamma_c$) and mantle ($\gamma_m$) radial anisotropy maps are illustrated in **Fig. 7a and 7b**. $\gamma_c$ are considered indeterminate if the estimated sedimentary thickness is greater than 3 km depth or the one standard deviation uncertainty is larger than 1.5 %. In the mantle, $\gamma_m$ > 2 % are considered as indeterminate. The grid points with indeterminate anisotropy are shown in grey color. The majority parts of the locations across the study region emerge with positive anisotropy in the crust and mantle, with very few exceptions. Locations with high elevations generally are associated with relatively smaller crustal anisotropy than their surrounding regions, including the Pyrenees and the Iberian Chain. However, one exception with high elevation but also strong anisotropy is the Betic mountains. In the mantle, the Northern Plateau and central eastern part of the Iberian Peninsula are identified with relatively large anisotropy. Strong mantle anisotropy also emerges beneath the Atlas Mountains and surroundings.

## 6. Discussion

In this section, I focus on discussion about the crustal and mantle anisotropy, including assessment of the reliability of the anisotropy model, and implications for crustal and mantle deformation.

### 6.1 Model Assessment: Reliability of the Inferred Anisotropy

In order to reliably determine radial anisotropy ($\gamma_c$, $\gamma_m$), both Vsv and Vsh need to be simultaneously resolved by the inversion. To assess the quality of Vsv part of the model, I inspect the posterior distributions of different model parameters at sample locations (**Figure 4**) and compare the Vsv slices (**Figure 5**) with existing tomographic studies. Assessment of the radial anisotropy ($\gamma_c$, $\gamma_m$) is done in a different way, because there is no high-resolution crustal anisotropy model for comparison and different mantle anisotropy models show poor agreement on regional scale (although a comparison of anisotropy models is done later for interpretation purposes). Inversions with different model parametrizations are performed to verify if the anisotropy parameters are well resolved by the data.

### 6.2.1 Vsv Structure

**Figure 4** presents inversion results at three sample stations, IB.E026, IB.M215 and X7.PE03, whose locations are identified in the inset of **Fig. 1a**. Vsv at intermediate depth of the crust and mantle can be well resolved by surface wave only inversion (SW) or the joint inversion incorporating receiver functions (SW+RF), as indicated by the posterior distributions of Vsv at 15 and 80 km depths. Besides, crustal thickness can also be resolved with SW inversion, while introducing receiver functions (SW+RF) further improves the constraints and reduces the associated uncertainties. The sample posterior distributions prove that the Vsv structures are reasonably resolved by the data.

The reliability of the Vsv part of the model can be further confirmed by comparing Vsv slices in this study (**Figure 5**) with existing tomographic models (e.g., Fichtner & Villaseñor, 2015; Palomeras et al., 2017). Lots of geological and tectonic features are consistently resolved by different tomographic models and here I list a few of them.

(1) The Iberian Massif is imaged with high Vsv in the crust (**Figure 5a, 5b and 5c**) but becomes a low-speed anomaly at ~ 100 km (**Figure 5f**). This feature is imaged by both Fichtner & Villaseñor (2015) and Palomeras et al. (2017).

(2) A Vsv contrast along the Toulouse Fault can be identified in the mantle (**Figure 5d, 5e and 5f**), with the western domain imaged as high Vsv anomaly and the Massif Central to the east emerges with low Vsv. This Vsv contrast is imaged in Fichtner & Villaseñor (2015)'s full-waveform inversion model and Chevrot et al. (2014)'s P-wave tomography model.

(3) Extremely low Vsv in the crust beneath the Betic-Rif belt is reported by Palomeras et al. (2017) and the underneath mantle part emerges with high Vsv, interpreted as the Alboran slab by Fichtner & Villaseñor (2015) and Palomeras et al. (2017).

(4) Low Vsv anomaly in the mantle beneath the Atlas Mountains is consistently resolved by different models (e.g., Fichtner & Villaseñor, 2015; Palomeras et al., 2017)

(5) The crustal thickness map (**Figure 6b**) is generally consistent with previous receiver function studies (e.g., de Lis Mancilla & Diaz, 2015). Besides, the regions with thick crust are associated with mountain ranges, including the Pyrenees, the Iberian Chain, the Betic-Rif Belt and the Atlas Mountains.

As a summary, the Vsv slices (**Figure 5**) resolve lots of major geological and tectonic features that are consistent with existing tomographic models, demonstrating the reliability of the Vsv part of the model.

#### 6.1.2 Radial anisotropy and Variance Reduction

As illustrated by **Figure 4b, 4h, and 4n**, Love wave dispersion curves cannot be reasonably fitted with isotropic profiles at the three sample stations. This is the well-known phenomenon called "Rayleigh-Love discrepancy". Namely, an isotropic Vs model cannot reasonably fit both Rayleigh and Love wave dispersion data. As shown by **Figure 8a**, an isotropic model produces widespread large misfit values across the study region, indicating the fact that the Rayleigh-Love discrepancy is broadly observed in the study region.

To resolve the Rayleigh-Love discrepancy, radial anisotropy is required. Radial anisotropy, also called polarization anisotropy (e.g., Moschetti et al., 2010), refers to the phenomenon that vertically polarized S waves ($V_{sv}$) have different wave speed compared with horizontally polarized S waves ($V_{sh}$). Because Rayleigh waves are mostly sensitive to $V_{sv}$ and Love waves are dominantly controlled by $V_{sh}$, therefore, the Rayleigh-Love discrepancy typically indicates existence of strong radial anisotropy ($V_{sv} \neq V_{sh}$).

As shown in **Figure 4b, 4h, and 4n**, by allowing radial anisotropy in the crust and mantle, Love wave dispersion curves can be fitted at all the sample stations. Moschetti et al. (2010) and Feng & Ritzwoller (2019) showed that there is a negative trade-off relationship between crustal and mantle anisotropy. Indeed, as illustrated by **Figure 4f, 4l, and 4r,** negative trade-offs between the crustal and mantle anisotropy are observed all sample locations. The inferred amplitudes of both crustal and mantle anisotropy could be affected by the trade-off and thus special care much be taken when building a radial anisotropy model. The anisotropy trade-off naturally raises a question: Do we really need both crustal and mantle anisotropy to fit the data?

To answer this question, I perform two additional inversions, one only allows radial anisotropy in the crust and another with anisotropy confined in the mantle. **Figure 8c and Figure 8d** show the misfit maps corresponding to the mantle anisotropy only and crustal anisotropy only inversions. By inspecting the misfit maps, three conclusions can be drawn:

(1) Incorporating anisotropy in the crust or mantle can improve data fitness and resolve the Rayleigh-Love discrepancy (**Figure 8c and Figure 8d**), while the best data fitting is achieved by allowing both crust and mantle to be anisotropic (**Figure 8b**).
(2) The patterns of the crustal and mantle misfit maps (**Figure 8c and Figure 8d**) are generally similar to the crustal and mantle anisotropy maps (**Figure 7**). The similarities imply that inferred anisotropy is indeed required by the data.
(3) Crustal anisotropy brings more variance reduction than the mantle anisotropy, this implies that crustal anisotropy is determined more reliably. Indeed, as also shown by the anisotropy trade-off figures (**Figure 4f, 4l, and 4r**), non-zero crustal anisotropy is generally required by almost all the accepted models.

The advantage of the Bayesian Monte Carlo inversion is that uncertainties of model parameters are produced, which could be naturally used to as references to tell us how much we should believe the model or which part of the model is more believable. The uncertainty estimates are used to identify indeterminate grid points in **Figure 7**, in which crustal anisotropy is considered indeterminate if the associated uncertainty is > 1.5 % and an uncertainty threshold value of 2 % is used to discard indeterminate points in the mantle anisotropy map. In addition, the laminated structures in sedimentary basins can produce strong radial anisotropy (e.g., Feng & Ritzwoller, 2019), the SPO (shape-preferred orientation) sediments could bias the estimation of anisotropy in the crystalline crust when the sedimentary layer is thick enough. Therefore, in the crustal anisotropy map (**Figure 7a**), grid points associated with large sedimentary thickness (> 3 km) are also identified as indeterminate and colored in grey.

As a summary, I conclude that the anisotropic part ($\gamma$) of the model is overall reliable and justified by the data. Because crustal anisotropy brings more variance reduction, hence it may be more reliable than the inferred mantle anisotropy.

### 6.2 Identifying Cenozoic Extension with Crustal Anisotropy

**Figure 7a** shows that positive crustal anisotropy is broadly distributed across the westernmost Mediterranean, with very few exceptions associated with very weak negative radial anisotropy ($V_{sv} > V_{sh}$). I focus on the interpretation of positive anisotropy in this subsection.

Widespread positive crustal radial anisotropy has been reported at different locations of the Earth, including the Basin and Range Province (e.g., Moschetti et al., 2010), Alaska (e.g., Feng & Ritzwoller, 2019) and Tibet (e.g., Shapiro et al., 2004). Existing studies typically attribute the observed crustal anisotropy to the LPO (lattice-preferred orientation) of mica-rich foliated metamorphic rocks because they are abundant in the crystalline crust. Besides, laboratory experiments (e.g., Lloyd et al., 2009) have shown that single crystal mica is one of the most anisotropic crustal minerals. The laminated sheets of single crustal mica making it possible to describe the crystal as transversely isotropic (TI) media, also called hexagonal symmetric media in some previous studies (e.g., Xie et al., 2015). The TI media has a symmetry axis and can be fully described by five elastic parameters if the alignment of the symmetry axis is assuming vertically oriented. The TI assumption remains a valid approximation for a variety types of mica-rich rock samples (e.g., Lloyd et al., 2009; Brownlee et al., 2017). Another possible candidate that may also play an important role contributing to the observed seismic anisotropy is amphibole (e.g., Tatham et al., 2008). However, single crystal amphibole has weaker anisotropy than mica and the rock samples abundant in amphibole typically exhibit as orthorhombic media (Brownlee et al., 2017), which could not be described by radial anisotropy. Other continental crustal minerals that may contribute to seismic anisotropy are quartz and feldspars, but in a destructive way. Experimental results (e.g., Ward et al., 2012) have shown that quartz and feldspars are not likely to produce a LPO induced anisotropy but could dilute the anisotropic strength of the mica-bearing rocks. As a summary, the observed anisotropy (**Figure 7a**) most likely originates from the mica-rich rocks, however, it is hard to rule out the contribution from other types of crustal composition.

Despite of the complexity in the composition of the anisotropic rocks, the relationship between strong radial anisotropy and crustal deformation is probably more straightforward. For example, Shapiro et al. (2004) reported that the radial anisotropy is largely controlled by channel flow in the mid-to-lower crust in Tibet, which is associated to crustal thinning. Similar relationship between radial anisotropy and crustal thinning has been found at the Basin and Range Province by Moschetti et al. (2010), in which the authors reported that the observed widespread radial anisotropy is mostly confined to the region undergone significant extension during the Cenozoic Era. However, the relationship between radial anisotropy and crustal thinning may not always be valid. For instance, in Alaska, Feng & Ritzwoller (2019) reported that the radial anisotropy is strong at the southern parts of the Brooks Range, the Yukon composite Terrane, the Seward Peninsula and the Ruby Terrane. These places have been identified as regions undergone significant mid-Cretaceous extension, which were called as the "hinterland" by Miller & Hudson (1991). Although relatively thin crust has been found at the Yukon composite Terrane, the Seward Peninsula and the Ruby Terrane, however, thick crust beneath the Brooks Range has reported by Feng & Ritzwoller (2019) and receiver function studies (e.g., Miller & Moresi, 2018). In a nutshell, strong radial anisotropy in the crust is generally associated with extensional deformation, it may also be related to relatively thin crust and low topography, but there are exceptions (e.g., Feng & Ritzwoller, 2019).

To better locate the areas with strong crustal radial anisotropy, I produce a map (**Figure 9a)** identifying regions with relatively strong crustal anisotropy in blue ($\gamma_c > 3.5\%$). The "blue" area is overall consistent with locations with Cenozoic outcrops (Arroucau et al., 2021), which may have undergone extensional deformation during the Cenozoic Era. Strong crustal anisotropy is overall associated with thinner crust (**Fig. 6b**), with one exception beneath the Betic mountains. According to the distribution of crustal anisotropy, I mark the regions that probably have undergone Cenozoic extension with blue arrows in **Figure 9a**.

De Vincente et al. (2009) presented a tectonic model reconstructing the Africa-Iberia movement during the Cenozoic Era. From the early Oligocene to lower Miocene, the paleo-reconstructions (Rosenbaum et al., 2002) indicated that the Africa plate and the Iberian microplate came 115 km closer. Based on evidence from paleomagnetic studies (Muñoz-Martín et al., 2010), no significant relative motion has occurred at the boundary separating the Africa plate and the Iberian microplate since the Eocene. Compressive deformation (shortening) was transmitted to the interior of the plates leading to most topographical features of the Iberian Peninsula and Morocco, including the Pyrenees, the Iberian Chain, the Central Range, the Cantabrian Range and the Atlas Mountains.

These mountain ranges are associated with weaker crustal anisotropy (< 3.5%, **Fig. 7a, Fig. 9a**). Possible shortening locations from the early Oligocene to the lower Miocene are marked with red arrows in **Figure 9a**. The red arrow areas (shortening, associated with topographical features) and the blue arrow regions (extension, inferred from crustal anisotropy) constitute a "jigsaw fit" as a whole, which means that the crustal anisotropy distribution could serve as seismic evidence partially supporting De Vincente & Vegas (2009)'s model explaining the Cenozoic movement of the African plate and the Iberian microplate.

The only outliner which does not really fit in the above "jigsaw fit" is the Betics. However, there is clear evidence of lithospheric thinning in the center of the convergence belt (e.g., Molnar & Houseman, 2004). Convergence between the Eurasian and African plate during the late Cretaceous and the early Cenozoic produces the Betic-Rif belt, separated by the Alboran Sea in the center (Platt & Vissers 1989). The resolved high-Vsv anomalies in the mantle beneath the Betic-Rif belt (**Fig. 5d, 5e and 5f**) provide seismic evidence consistent with downwelling beneath the margins of a Cenozoic convergent zone (Molnar & Houseman, 2004). And the low-Vsv anomaly in the uppermost mantle ( < 100 km, **Fig. 5d and 5e**) beneath the Alboran Sea indicates lithospheric thinning and high temperatures in the middle of the convergent belt. Unlike other intraplate topographical features, the uplift of the Betics is produced from the convective removal of the lithosphere (Platt & Vissers 1989), which could be accompanied by crustal extension (Huismans & Beaumont, 2008) to produce strong radial anisotropy.

### 6.3 Mantle Anisotropy and Implications for Asthenospheric Flow

In the mantle, the dominant cause of anisotropy is the lattice-preferred orientation (LPO) of olivine fabrics (Montagner, 2007), as olivine is the most common upper mantle mineral with a strong single crystal anisotropy. Under different physical and chemical environments (e.g., pressure, temperature, water contents), different types of olivine fabrics can develop and the resulting radial anisotropy could differ in both magnitude and patterns. For A- and E-type olivine, the fast axes of the olivine crystals align in the direction of shear deformation and thus could be used as an indicator of mantle flow pattern (Karato et al., 2008). Under the assumption of A- or E-type olivine, a positive radial anisotropy ($V_{sh} > V_{sv}$) in the mantle indicates horizontal flow while a negative anisotropy ($V_{sh} < V_{sv}$) implies vertical flow (Karato et al., 2008). In global scale, radial anisotropy inferred from different tomography models has achieved good agreement providing a first-order relationship with mantle rheology (e.g., Becker et al., 2008). However, radial anisotropy models at regional scale, especially at locations with complex tectonics, typically shows poor agreement. This is also the case in the westernmost Mediterranean.

By inspecting the mantle anisotropy map (**Figure 7b**), strong radial anisotropy can be identified beneath eastern part of the Iberian Peninsula and the Atlas Mountains (**Figure 9b**). I denote these two places as region I and region II respectively. In terms of variance reduction (**Fig. 8b and 8d**), introducing mantle anisotropy improves data fitness more at region I, hence strong anisotropy beneath region I is probably more believable than region II. Note that the mantle anisotropy presented in this study reflects an average anisotropic response of the uppermost mantle, with depth ranges starting from the Moho and ending at 200 km depth.

Compared with Zhu & Tromp (2013)'s radially anisotropy model, region II is identified at similar mantle depth ranges (50 km, 100 km and 150 km depths), while region I only emerges in the 50 km slice from Zhu & Tromp (2013). In Fichtner & Villaseñor (2015)'s model, both region I and II can be identified in the 40, 70 and 100 km depth slices, however, the authors also reported a strong anisotropy spot beneath the Iberian Massif at 70 and 100 km depth, which is only partially seen in **Figure 7b** (southwestern corner of the Iberian Massif). Strong anisotropy amplitudes beneath region I and II are also reported by Schaefer et al. (2011)'s tomographic model and the authors' anisotropy model derived from geodynamical predictions. Based on the comparison with Schaefer et al. (2011)'s geodynamical model, I suggest that the large anisotropy beneath region I and II probably reflects strong horizontal mantle flow.

However, there are several caveats preventing me from interpreting the mantle anisotropy map further to discuss its tectonic implications. (1) As discussed earlier, there is a trade-off between crustal and mantle anisotropy and incorporating mantle anisotropy brings much less variance reduction compared with crustal anisotropy. Therefore, while crustal anisotropy presented in this study is overall reliable, the fidelity of mantle anisotropy degrades to some extent. (2) A simple uniform anisotropic mantle layer is assumed in the inversion, representing the average anisotropic response from the Moho to a depth of 200 km. Because of this, it is not quite clear whether the inferred anisotropy resides in the lithosphere or the asthenosphere. This could largely affect the geodynamical interpretation, because the anisotropy in the lithosphere is frozen-in, while the asthenospheric anisotropy reflects present-day mantle flow directions. One possible way to better justify and interpret the mantle radial anisotropy estimates here is to incorporate regional scale estimation of azimuthal anisotropy. By introducing azimuthal anisotropy (surface wave, SKS splitting) as additional data, inference of tilted-TI media can be performed (e.g., Xie et al., 2015) to provide more insights for the mantle deformation. Inversion for a tilted-TI model is beyond the scope of this paper.

## 7. Conclusions

In this study, I present a new 3-D radially anisotropic shear wave velocity model for the crust and uppermost mantle to a depth of 200 km beneath the westernmost Mediterranean, including southmost of France, the Iberian Peninsula and northern Morocco. The model is constructed from a joint Bayesian Monte Carlo inversion of Rayleigh and Love wave dispersion curves along with receiver functions. The Vsv structures imaged by the model are generally consistent with existing tomographic models (e.g., Fichtner & Villaseñor, 2015; Palomeras et al., 2017) and the crustal thickness map indicates thick crust associated with major mountain ranges. Radial anisotropy in the crust identifies regions that have undergone Cenozoic extension, which may help us better reconstruct the Africa-Iberia movement from the early Oligocene to the lower Miocene, leading to an improved understanding of the Cenozoic evolution of the western Mediterranean. Mantle anisotropy implies regions with strong horizontal mantle flow which is overall consistent with geodynamical predictions.

The anisotropic 3-D Vs model is a useful reference for a variety of purposes. It can be used as a reference for better understanding of the tectonic evolution of the westernmost Mediterranean and can also help predicting other types of seismic data, such as seismic amplification (Feng & Ritzwoller, 2017). In the future, incorporating observations from azimuthal anisotropy to infer a titled-TI model (e.g., Xie et al., 2015) is desirable, which could lead to an improved understanding of the deformational processes beneath this region.

## Acknowledgments

The author is grateful to several data centers (IRIS, ORFEUS, GEOFON, RESIF) which make their data available to the public. The network codes for data and corresponding DOI can be found in **Table S1**.

**References**

Arroucau, P., Custódio, S., Civiero, C., Silveira, G., Dias, N., Díaz, J., Villaseñor, A. and Bodin, T., 2021. PRISM3D: a 3-D reference seismic model for Iberia and adjacent areas. *Geophysical Journal International*, *225*(2), pp.789-810. https://doi.org/10.1093/gji/ggab005

Bensen, G.D., Ritzwoller, M.H., Barmin, M.P., Levshin, A.L., Lin, F., Moschetti, M.P., Shapiro, N.M. and Yang, Y., 2007. Processing seismic ambient noise data to obtain reliable broad-band surface wave dispersion measurements. *Geophysical Journal International*, *169*(3), pp.1239-1260. https://doi.org/10.1111/j.1365-246X.2007.03374.x

Bonnin, M., Nolet, G., Villasenor, A., Gallart, J. and Thomas, C., 2014. Multiple-frequency tomography of the upper mantle beneath the African/Iberian collision zone. *Geophysical Journal International*, *198*(3), pp.1458-1473. https://doi.org/10.1093/gji/ggu214

Brownlee, S. J., Schulte-Pelkum, V., Raju, A., Mahan, K., Condit, C., & Orlandini, O. F., 2017. Characteristics of deep crustal seismic anisotropy from a compilation of rock elasticity tensors and their expression in receiver functions. *Tectonics*, 36, 1835–1857. https://doi.org/10.1002/2017TC004625

de Lis Mancilla, F. and Diaz, J., 2015. High resolution Moho topography map beneath Iberia and Northern Morocco from receiver function analysis. *Tectonophysics*, *663*, pp.203-211. https://doi.org/10.1016/j.tecto.2015.06.017

De Vicente, G. and Vegas, R., 2009. Large-scale distributed deformation controlled topography along the western Africa–Eurasia limit: Tectonic constraints. *Tectonophysics*, *474*(1-2), pp.124-143. doi:10.1016/j.tecto.2008.11.026

Di Bucci, D., P. Burrato, P. Vannoli, and G. Valensise, 2010. Tectonic evidence for the ongoing Africa-Eurasia convergence in central Mediterranean foreland areas: A journey among long-lived shear zones, large earthquakes, and elusive fault motions, *Journal of Geophysical Research: Solid Earth*, *115*, B12404, doi:10.1029/2009JB006480.

Faccenna, C., Piromallo, C., Crespo-Blanc, A., Jolivet, L., and Rossetti, F., 2004. Lateral slab deformation and the origin of the western Mediterranean arcs, *Tectonics*, 23, TC1012, doi:10.1029/2002TC001488.

Faccenna, C., Becker, T.W., Auer, L., Billi, A., Boschi, L., Brun, J.P., Capitanio, F.A., Funiciello, F., Horvath, F., Jolivet, L., Piromallo, C., Royden, L.H., Rossetti, F., Serpelloni, E., 2014. Mantle dynamics in the Mediterranean. *Reviews of Geophysics*, 52, 283–332. https://doi.org/10.1002/2013RG000444

Feng, L. and Ritzwoller, M.H., 2017. The effect of sedimentary basins on surface waves that pass through them, *Geophysical Journal International*, 211(1), 572-592, doi:10.1093/gji/ggx313.

Feng, L., and Ritzwoller, M.H., 2019. A 3-D shear velocity model of the crust and uppermost mantle beneath Alaska including apparent radial anisotropy, *Journal of Geophysical Research: Solid Earth*, 124, 19,468-10,497, doi.org/10.1029/2019JB018122.

Feng, L., Liu, C. and Ritzwoller, M.H., 2020. Azimuthal Anisotropy of the Crust and Uppermost Mantle beneath Alaska. *Journal of Geophysical Research: Solid Earth*, *125*(12), p.e2020JB020076.

Feng, L. 2021. High-resolution crustal and uppermost mantle structure beneath central Mongolia from Rayleigh waves and receiver functions. *Journal of Geophysical Research: Solid Earth*, 126, e2020JB021161. *https://doi.org/10.1029/2020JB021161*

Huismans, R.S. and Beaumont, C., 2008. Complex rifted continental margins explained by dynamical models of depth-dependent lithospheric extension. *Geology*, *36*(2), pp.163-166. https://doi.org/10.1130/G24231A.1

Karato, S.I., Jung, H., Katayama, I. and Skemer, P., 2008. Geodynamic significance of seismic anisotropy of the upper mantle: New insights from laboratory studies. *Annual Review of Earth and Planetary Sciences*, *36*, pp.59-95.

Kennett B. L. N., Engdahl E. R. and Buland R. 1995. Constraints on seismic velocities in the earth from travel times. *Geophysical Journal International 122*:108-124. https://doi.org/10.1111/j.1365-246X.1995.tb03540.x

Koulali, A., Ouazar, D., Tahayt, A., King, R.W., Vernant, P., Reilinger, R.E., McClusky, S., Mourabit, T., Davila, J.M. and Amraoui, N., 2011. New GPS constraints on active deformation along the Africa–Iberia plate boundary. *Earth and Planetary Science Letters*, *308*(1-2), pp.211-217. https://doi.org/10.1016/j.epsl.2011.05.048

Laske, G., Masters., G., Ma, Z. and Pasyanos, M., 2013. Update on CRUST1.0 - A 1-degree Global Model of Earth's Crust, *Geophysical Research Abstracts, 15*, Abstract EGU2013-2658.

Laville, E., A. Pique, M. Amrhar, and M. Charroud, 2004. A restatement of the Mesozoic Atlasic Rifting (Morocco), *Journal African Earth Sciences, 38*, 145– 153, doi:10.1016/j.jafrearsci.2003.12.003.

Ligorria, J.P. and Ammon, C.J., 1999. Iterative deconvolution and receiver-function estimation. *Bulletin of the seismological Society of America, 89*(5), pp.1395-1400.

Lin, F.C., Ritzwoller, M.H. and Snieder, R., 2009. Eikonal tomography: surface wave tomography by phase front tracking across a regional broad-band seismic array. *Geophysical Journal International, 177*(3), 1091-1110. https://doi.org/10.1111/j.1365-246X.2009.04105.x

Lin, F.C. and Ritzwoller, M.H., 2011. Helmholtz surface wave tomography for isotropic and azimuthally anisotropic structure. *Geophysical Journal International, 186*(3), pp.1104-1120. https://doi.org/10.1111/j.1365-246X.2011.05070.x

Lloyd, G. E., Butler, R. W., Casey, M., & Mainprice, D. 2009. Mica, deformation fabrics and the seismic properties of the continental crust. *Earth and Planetary Science Letters, 288*(1–2), 320–328. https://doi.org/10.1016/j.epsl.2009.09.035

Lonergan, L. and White, N., 1997. Origin of the Betic-Rif mountain belt. *Tectonics*, *16*(3), pp.504-522.

Michard, A., Soulaimani, A., Hoepffner, C., Ouanaimi, H., Baidder, L., Rjimati, E.C. and Saddiqi, O., 2010. The south-western branch of the Variscan Belt: evidence from Morocco. *Tectonophysics*, *492*(1-4), pp.1-24. https://doi.org/10.1016/j.tecto.2010.05.021

Miller, E. L., & Hudson, T. L. 1991. Mid-Cretaceous extensional fragmentation of the Jurassic-Early Cretaceous compressional orogeny, Alaska. *Tectonics, 10*(4), 781–796. https://doi.org/10.1029/91TC00044

Miller, M. S., & Moresi, L. 2018. Mapping the Alaskan Moho. *Seismological Research Letters, 89*(6), 2439–2436. https://doi.org/10.1785/ 0220180222

Molnar,P. and Houseman, G.A. 2004. The effects of buoyant crust on the gravitational instability of thickened mantle lithosphere at zones of intracontinental convergence, *Geophysical Journal International*, *158*(3), pp. 1134–1150, https://doi.org/10.1111/j.1365-246X.2004.02312.x

Moschetti, M.P., Ritzwoller, M.H., Lin, F. and Yang, Y., 2010. Seismic evidence for widespread western-US deep-crustal deformation caused by extension. *Nature*, *464*(7290), pp.885-889. https://doi.org/10.1038/nature08951

Montagner, J.P., 2007. Upper mantle structure: Global isotropic and anisotropic elastic tomography. *Treatise on geophysics*, *1*, pp.559-589.

Muñoz-Martín, A., De Vicente, G., Fernández-Lozano, J., Cloetingh, S.A.P.L., Willingshofer, E., Sokoutis, D. and Beekman, F., 2010. Spectral analysis of the gravity and elevation along the western Africa–Eurasia plate tectonic limit: Continental versus oceanic lithospheric folding signals. *Tectonophysics*, *495*(3-4), pp.298-314. https://doi.org/10.1016/j.tecto.2010.09.036

Nolet, G., 1977. The upper mantle under western Europe inferred from the dispersion of Rayleigh modes. *Journal of Geophysics*, *43*(1), pp.265-285.

Palomeras, I., Villaseñor, A., Thurner, S., Levander, A., Gallart, J. and Harnafi, M., 2017. Lithospheric structure of Iberia and Morocco using finite-frequency Rayleigh wave tomography from earthquakes and seismic ambient noise. *Geochemistry, Geophysics, Geosystems*, *18*(5), pp.1824-1840. https://doi.org/10.1002/2016GC006657

Pawlewicz, M.J., Steinshouer, D.W. and Gautier, D.L., 1997. *Map showing geology, oil and gas fields, and geologic provinces of Europe including Turkey* (No. 97-470-I). US Geological Survey.

Platt, J.P. & Vissers, R.L.M., 1989. Extensional collapse of thickened continental lithosphere: a working hypothesis for the Alboran Sea and Gibraltar Arc, *Geology, 17*, 540–543. https://doi.org/10.1130/0091-7613(1989)017%3C0540:ECOTCL%3E2.3.CO;2

Ritzwoller, M.H. and Feng, L., 2019. Overview of pre- and post-processing of ambient noise correlations, In N. Nakata, L. Gualtieri, and A. Fichtner (Eds.), Ambient Seismic Noise (pp. 144-187), Cambridge, *Cambridge University Press*, doi:10.1017/9781108264808.007.

Rosenbaum, R., Lister, G.S., Duboz, C., 2002. Relative motions of Africa, Iberia and Europe during Alpine orogeny. *Tectonophysics, 359*, 117–129. https://doi.org/10.1016/S0040-1951(02)00442-0

Schaefer, J.F., Boschi, L., Becker, T.W. and Kissling, E., 2011. Radial anisotropy in the European mantle: Tomographic studies explored in terms of mantle flow. *Geophysical research letters*, *38*(23). https://doi.org/10.1029/2011GL049687

Shapiro, N. M., Ritzwoller, M. H., Molnar, P., & Levin, V., 2004. Thinning and flow of Tibetan crust constrained by seismic anisotropy. *Science*, *305*(5681), 233–236. https://doi.org/10.1126/science.1098276

Shen, W**.**, Ritzwoller, M.H., Schulte-Pelkum, V. and Lin, F.C., 2012. Joint inversion of surface wave dispersion and receiver functions: a Bayesian Monte-Carlo approach. *Geophysical Journal International*, *192*(2),.807-836. https://doi.org/10.1093/gji/ggs050

Spakman, W. and Wortel, R., 2004. A tomographic view on western Mediterranean geodynamics. In *The TRANSMED atlas. The Mediterranean region from crust to mantle* (pp. 31-52). Springer, Berlin, Heidelberg. https://doi.org/10.1007/978-3-642-18919-7_2

Tatham, D.J., Lloyd, G.E., Butler, R.W.H., Casey, M., 2008. Amphibole and lower crustal seismic properties. *Earth and Planetary Science Letters, 267*, 118–128. https://doi.org/10.1016/j.epsl.2007.11.042

Becker, T.W., Kustowski, B. and Ekström, G., 2008. Radial seismic anisotropy as a constraint for upper mantle rheology. *Earth and Planetary Science Letters*, *267*(1-2), pp.213-227. https://doi.org/10.1016/j.epsl.2007.11.038

van der Voo., 1982. Pre-Mesozoic paleomagnetism and plate tectonics. *Annual Review of Earth and Planetary Sciences*, *10*(1), pp.191-220.

van Hinsbergen, D. J. J., R. L. M. Vissers, and W. Spakman, 2014. Origin and consequences of western Mediterranean subduction, rollback, and slab segmentation, *Tectonics, 33*, 393–419, doi:10.1002/2013TC003349.

Vergés, J. and Fernàndez, M., 2012. Tethys–Atlantic interaction along the Iberia–Africa plate boundary: The Betic–Rif orogenic system. *Tectonophysics*, *579*, pp.144-172. https://doi.org/10.1016/j.tecto.2012.08.032

Ward, D., K. Mahan, and V. Schulte-Pelkum, 2012, Roles of quartz and mica in seismic anisotropy of mylonites, *Geophysical Journal International*, *190*(2), 1123–1134, doi:10.1111/j.1365-246X.2012.05528.x.

Xie, J., Ritzwoller, M.H., Brownlee, S.J. and Hacker, B.R., 2015. Inferring the oriented elastic tensor from surface wave observations: preliminary application across the western United States. *Geophysical Journal International*, *201*(2), 996-1021. https://doi.org/10.1093/gji/ggv054

Zhang, S., Feng, L. and Ritzwoller, M.H., 2020. Three-station interferometry and tomography: coda versus direct waves. *Geophysical Journal International*, *221*(1), pp.521-541. https://doi.org/10.1093/gji/ggaa046

Zhu, H. and Tromp, J., 2013. Mapping tectonic deformation in the crust and upper mantle beneath Europe and the North Atlantic Ocean. *Science*, *341*(6148), pp.871-875. https://doi.org/10.1126/science.1241335

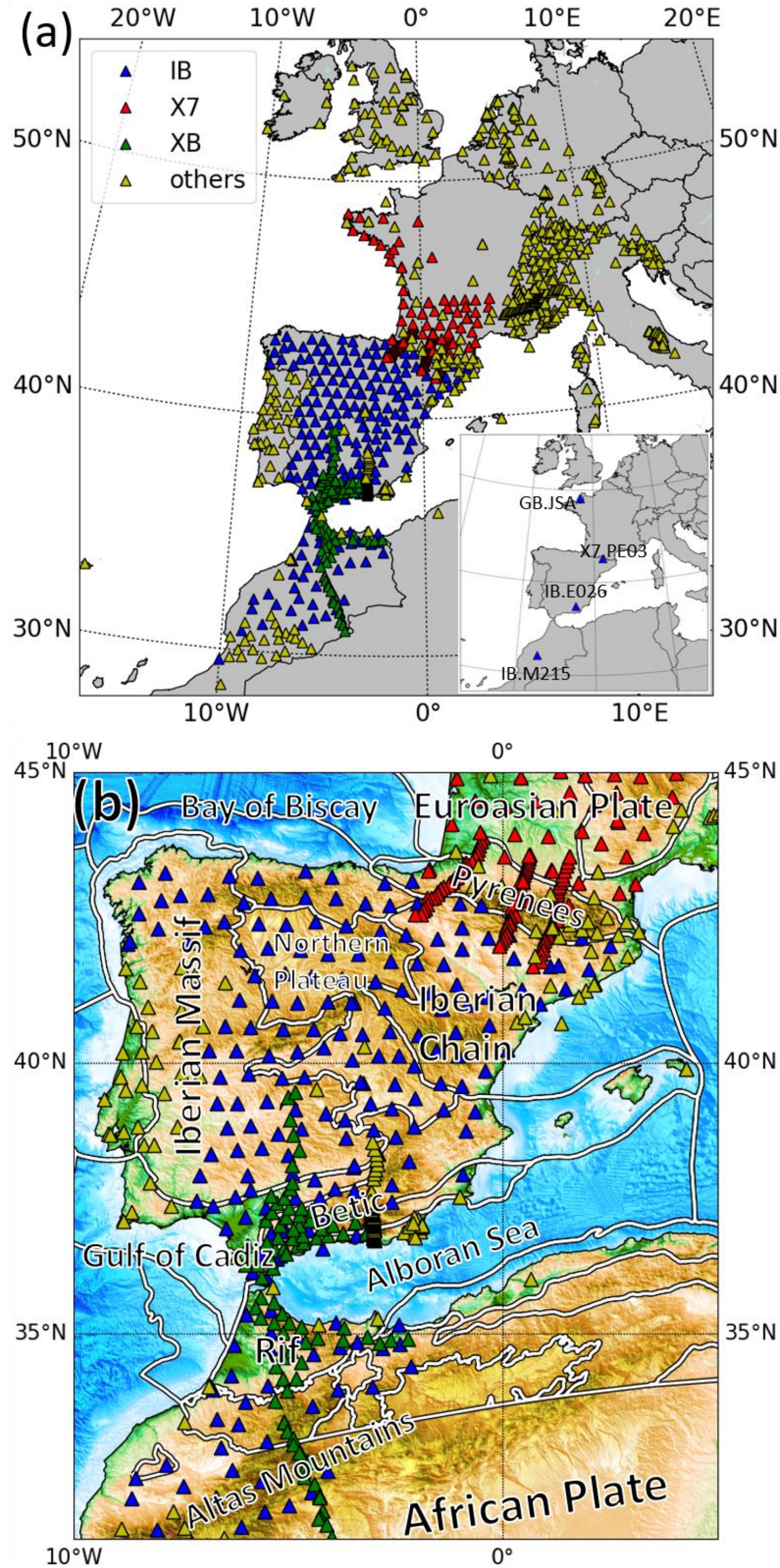
(a)
IB
X7
XB
others
20°W
10°W
0°
10°E
20°E
50°N
40°N
30°N
GB.JSA
X7.PE03
IB.E026
IB.M215
(b)
Bay of Biscay
Euroasian Plate
Pyrenees
Northern
Plateau
Iberian
Chain
Iberian Massif
Betic
Gulf of Cadiz
Alboran Sea
Rif
Altas Mountains
African Plate
45°N
35°N
10°W

**Figure 1.** (a) Station distribution map. The stations are colored with blue (IB, IberArray), red (X7, PYROPE array), green (XB, PICASSO array) and yellow (other networks). There are in total 1186 stations. The inset map identifies the locations of four sample stations used in **Figure 2** and **Figure 4**. (b) A topographic map of westernmost Mediterranean. White curves with black edges identify major geological provinces (Pawlewicz et al., 1997).

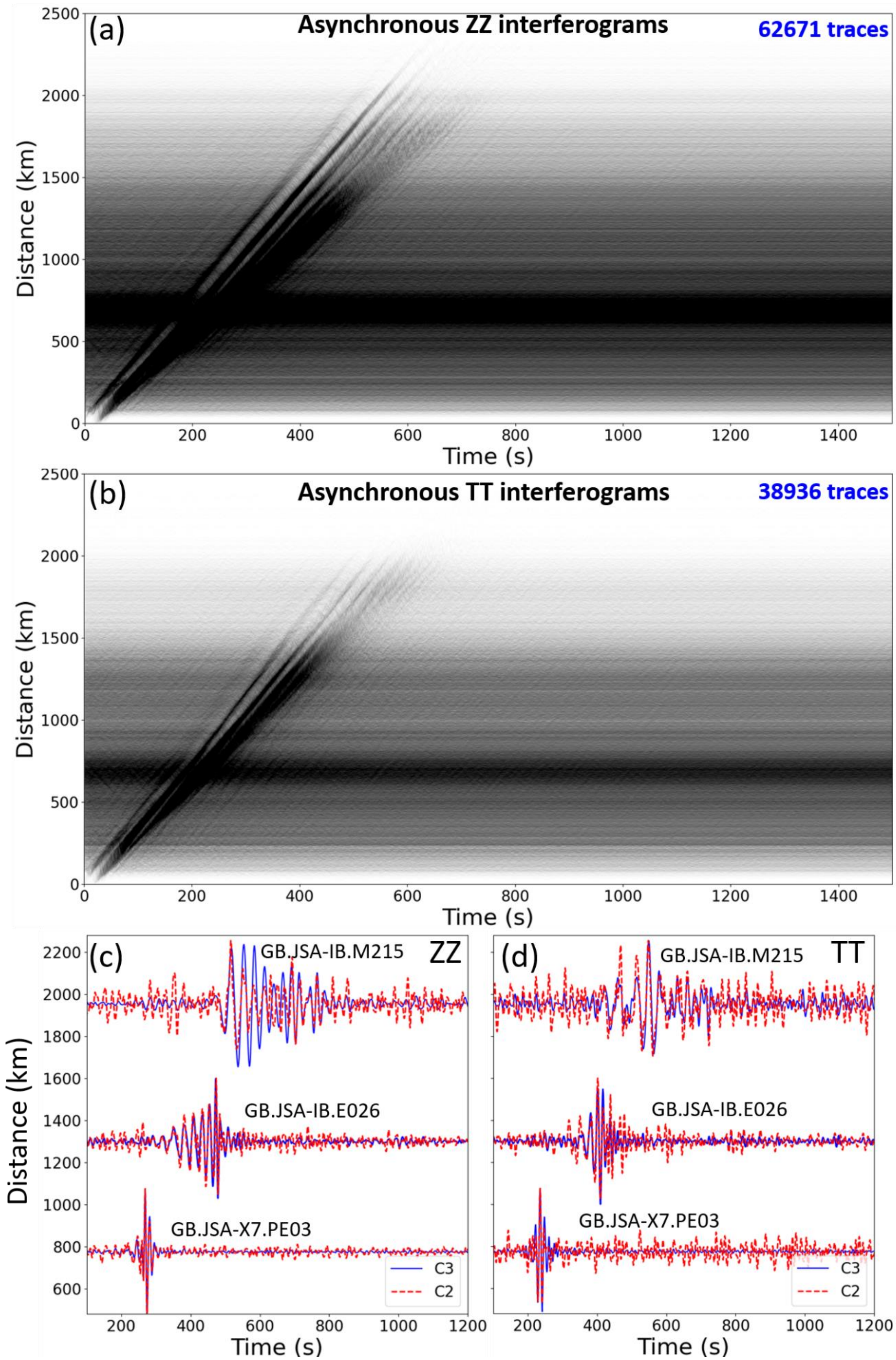
(a)
Asynchronous ZZ interferograms
62671 traces
Distance (km)
Time (s)
(b)
Asynchronous TT interferograms
38936 traces
Distance (km)
Time (s)
(c)
ZZ
GB.JSA-IB.M215
GB.JSA-IB.E026
GB.JSA-X7.PE03
C3
C2
Distance (km)
Time (s)
(d)
TT
GB.JSA-IB.M215
GB.JSA-IB.E026
GB.JSA-X7.PE03
C3
C2
Time (s)

728

**Figure 2.** (a) Asynchronous three-station interferograms of ZZ component. Each selected station pair includes at least one station belongs to the IB, XB or X7 networks. Number of traces are marked on the figure. (b) Same as (a), but for TT component. (c) Two- and three-station interferograms of ZZ component for three sample station pairs. Amplitudes are normalized in each interferogram. Locations of the sample stations are identified in the inset of **Fig. 1a**. (d) Same as (c), but for TT component.

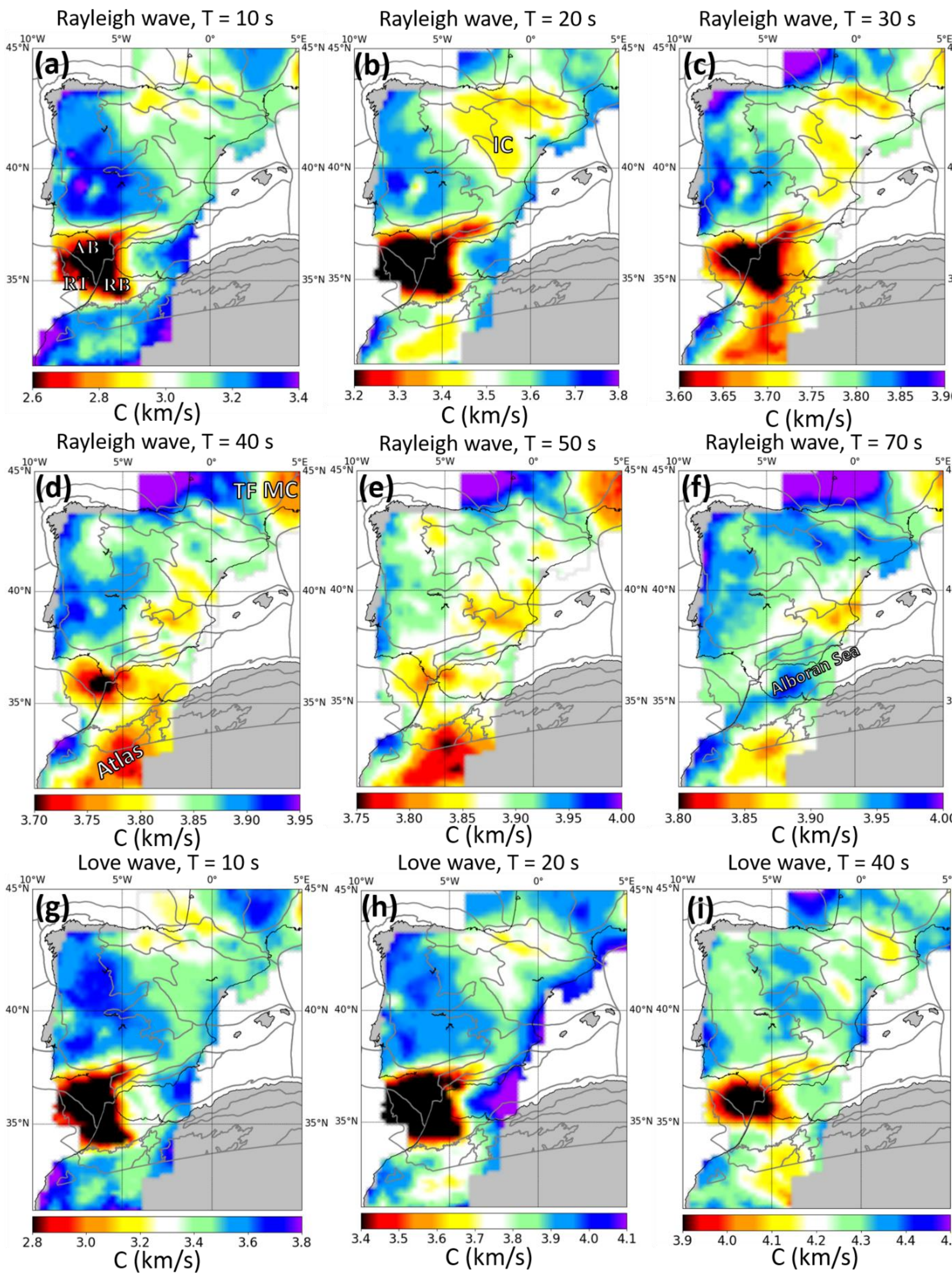


**Figure 3.** (a) – (f) Example Rayleigh wave phase velocity maps for T = 10 ~ 70 s periods. (g)-(i) Sample Love wave phase speed maps for T = 10 ~ 40 s periods. The grey curves identify major

geological provinces (Pawlewicz et al., 1997). The locations of the Alentejo-Guadalquivir Basin (AB), the Rabat Basin (RB) and the Rif Basin (RB) are identified in (a). In (b): IC: Iberian Chain. In (c) TF: Toulouse Fault; MC: Massif Central.

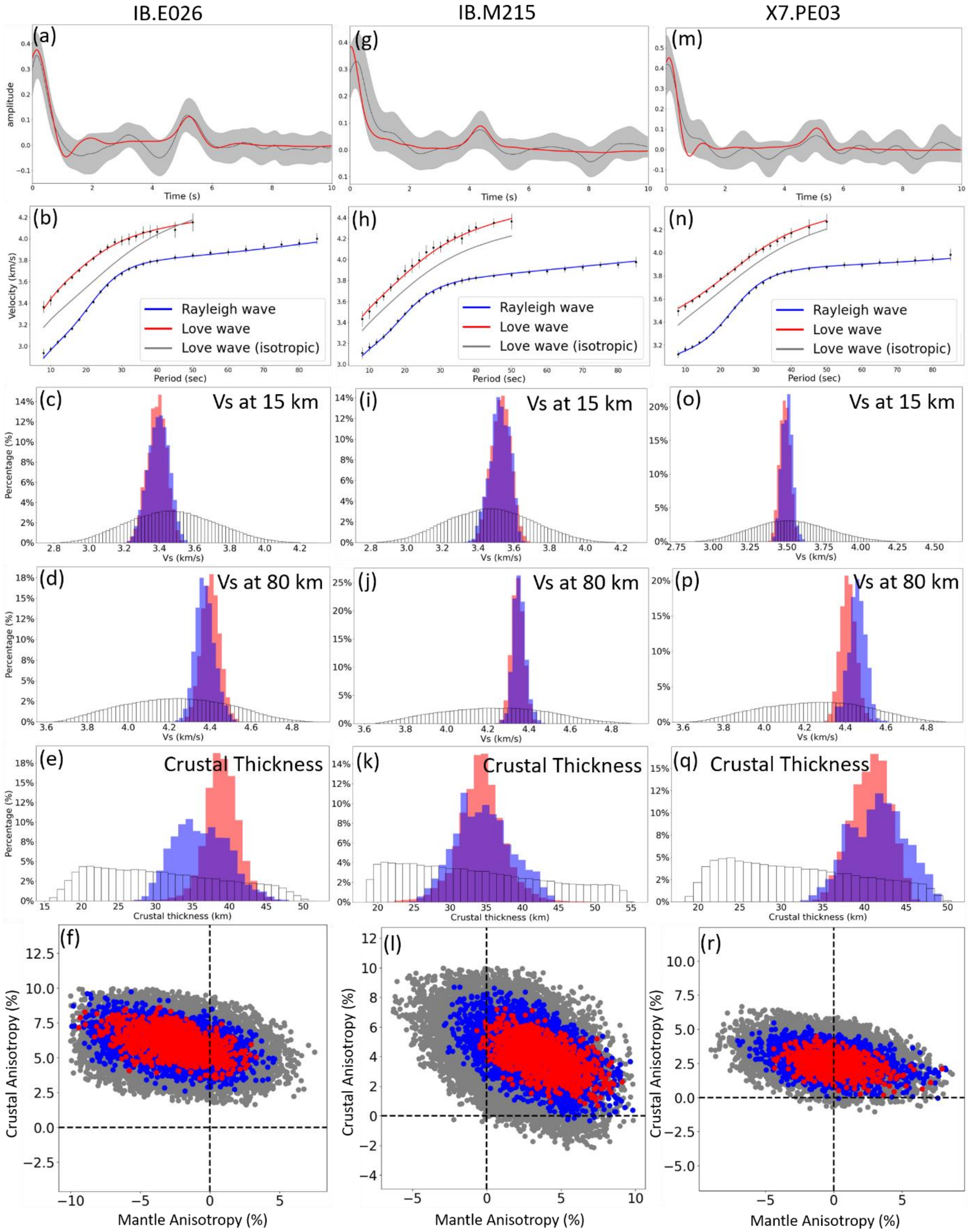

**Figure 4.** Example inversion results at three sample stations IB.E026, IB.M215 and X7.PE03. Locations of the sample stations are identified in the inset of **Fig. 1a**. (a) Receiver function fitness at IB.E026. The grey shaded area represents the one standard deviation uncertainty and the red curve is the predicted receiver function. (b) Data fitness for Rayleigh and Love waves at IB.E026. The dots with error bars represent observed Rayleigh and Love wave dispersion curves and the grey curve is the Love wave dispersion curve predicted from an isotropic model that best fits Rayleigh wave data. (c) Prior and posterior distributions of Vsv at 15 km depth. The white histogram represents the prior distribution and the blue histogram denotes result from inversion with surface wave data only (SW). Red histogram results from the joint inversion of surface wave and receiver function (SW+RF). (d) Same as (c), but for Vsv at 80 km depth. (e) Same as (c) and (d), but for crustal thickness. (f) Trade-off between crustal and mantle anisotropy. Symbol color indicates misfit value ($\chi$) at different ranges. Red: $\chi < \chi_{min} + 0.2$, blue: $\chi_{min} + 0.2 < \chi < \chi_{min} + 0.3$, grey: $\chi_{min} + 0.3 < \chi < \chi_{min} + 0.5$. (g) – (l): Same as (a) – (f), but for station IB.M215. (m) – (r): Same as (a) – (f), but for station X7.PE03.

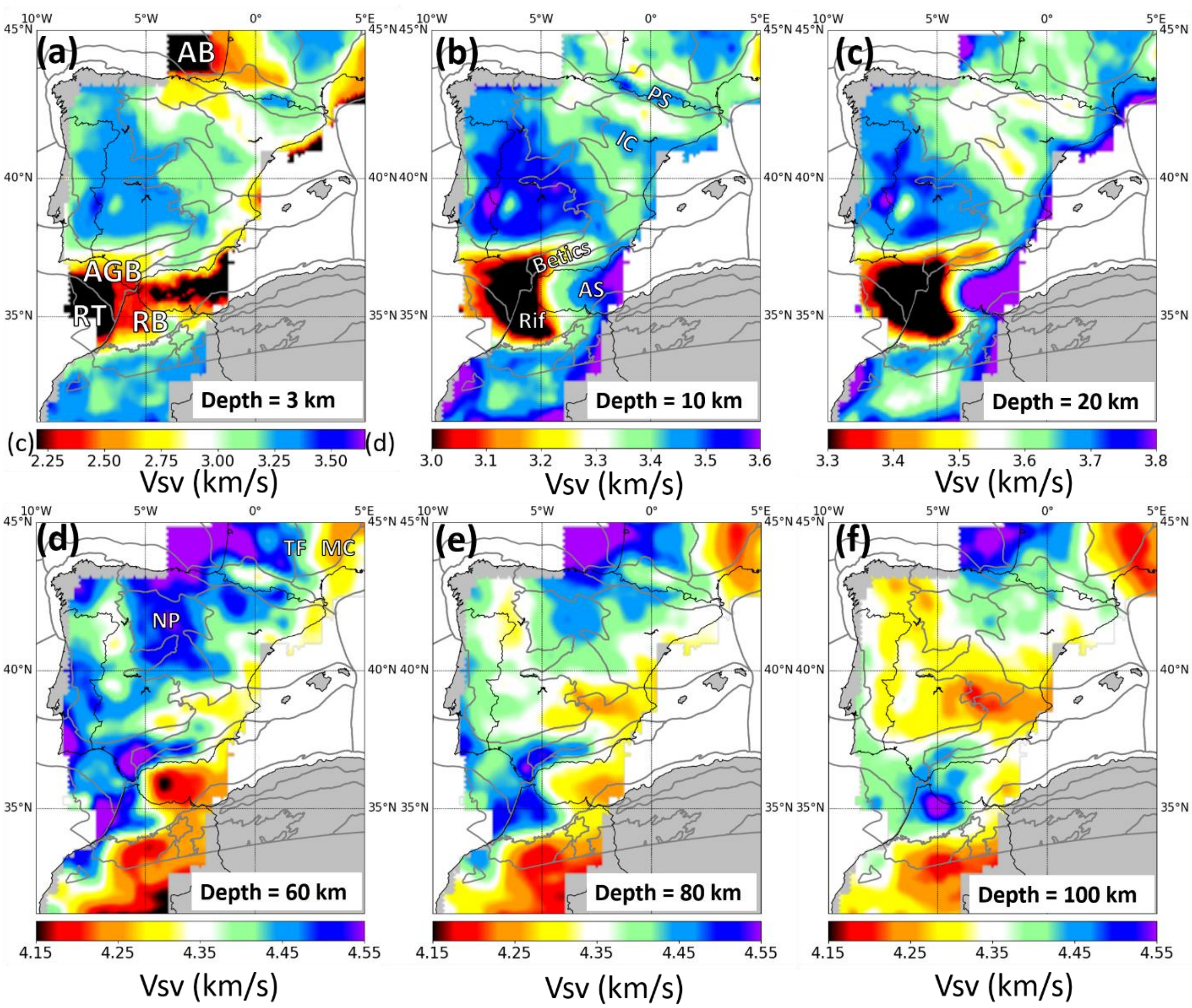


**Figure 5.** Sample Vsv slices at the depth of 3 km, 10 km, 20 km, 60 km, 80 km and 100 km (central-depth $\pm$ 3 $km$). In (a), major sedimentary basins are identified with abbreviations: AB:

Aquitaine Basin; AGB: Alentejo-Guadalquivir Basin; RT: Rabat Basin; RB: Rif Basin. In (b), PS: Pyrenees; IC: Iberian Chain; AS: Alboran Sea. In (d), MC: Massif Central; TF: Toulouse Fault; NP: Northern Plateau.

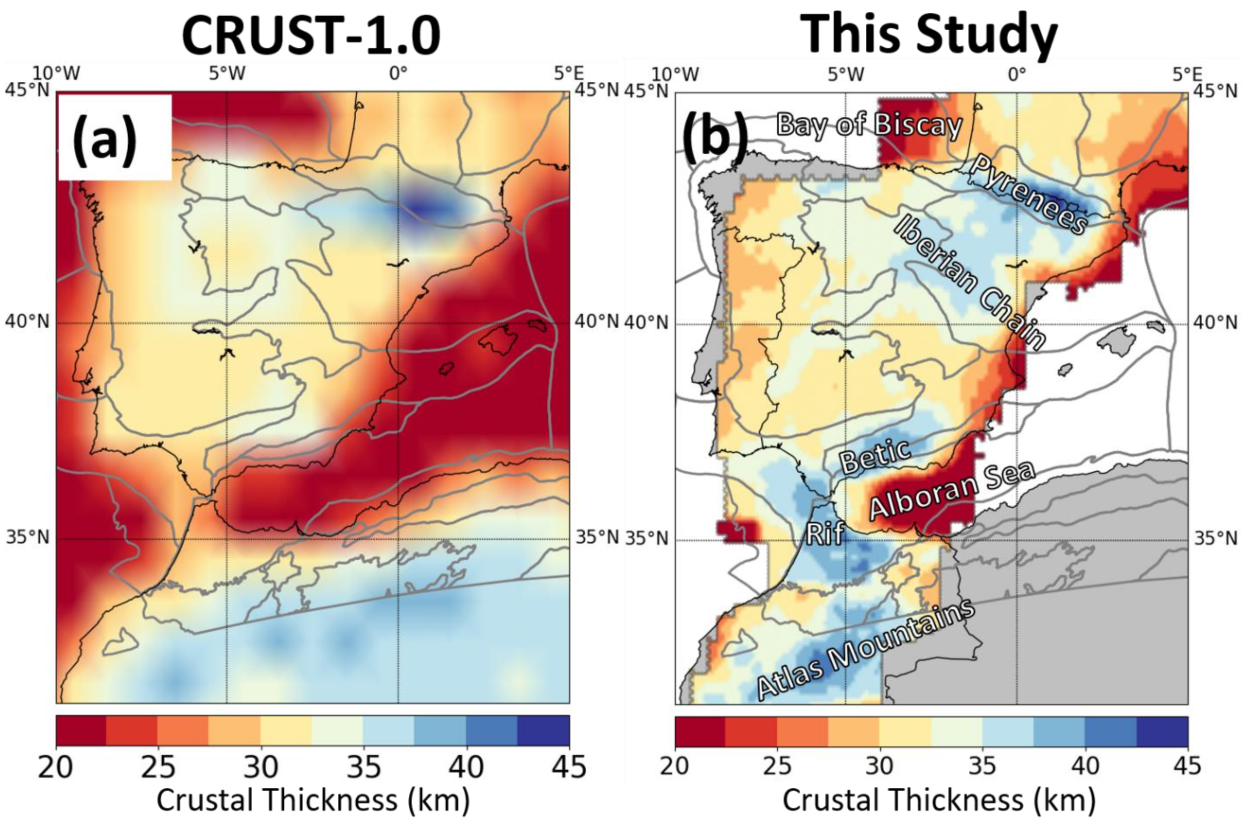


**Figure 6**. (a) CRUST-1.0 model. (b) Crustal thickness map constructed from this study.

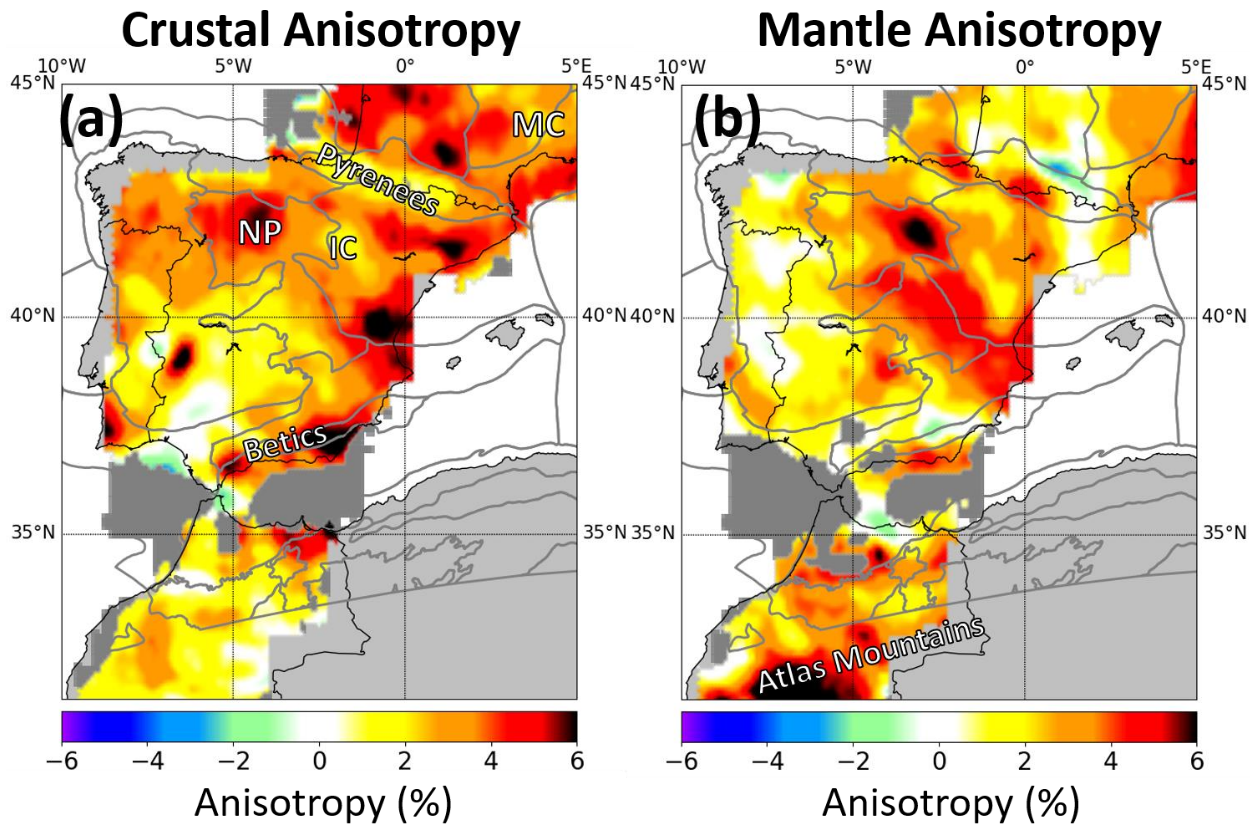


**Figure 7**. (a) Radial anisotropy in the crust. IC: Iberian Chain, NP: Northern Plateau, MC: Massif Central. (b) Radial anisotropy in the mantle. Grid points with indeterminate value of anisotropy are not shown and colored in grey.

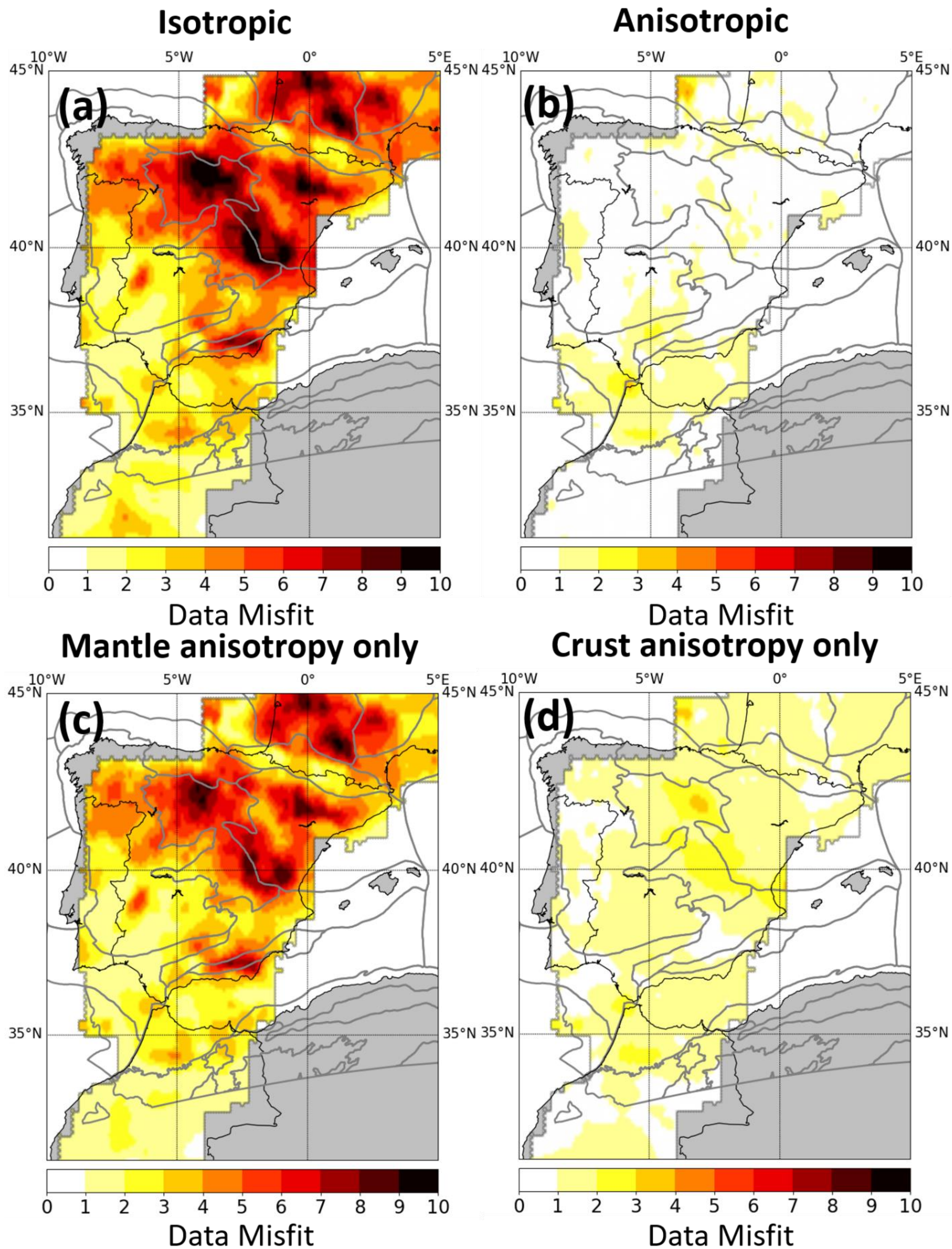
Isotropic
Anisotropic
Mantle anisotropy only
Crust anisotropy only
(a)
(b)
(c)
(d)
10°W
5°W
0°
5°E
45°N
40°N
35°N
0 1 2 3 4 5 6 7 8 9 10
Data Misfit

779

**Figure 8**. Misfit maps for different models. (a) Isotropic model. (b) Two-layer anisotropic model. (c) Model with anisotropy confined in the mantle only. (d) Model with anisotropy confined in the crust only.

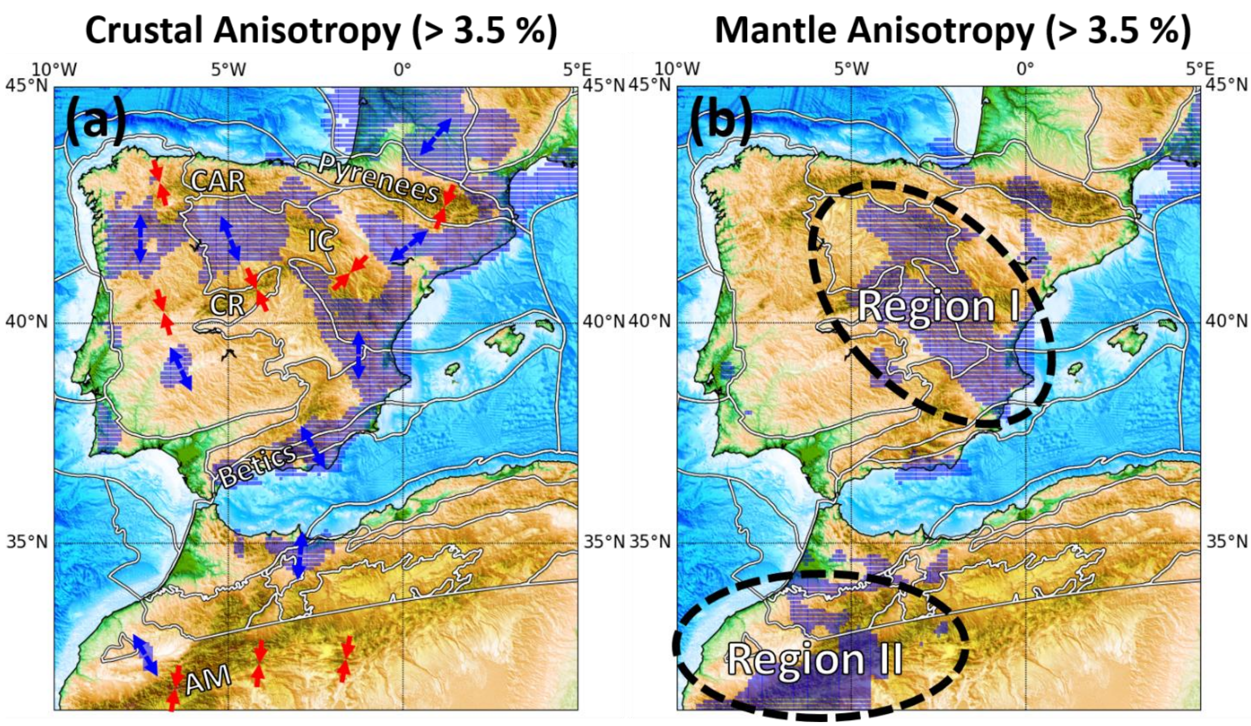


**Figure 9.** Regions (colored in blue) identified with strong anisotropy in the crust (a) and mantle (b). In (a), red arrows denote regions experienced shortening from the early Oligocene to the lower Miocene, including Pyrenees, the Iberian Chain, the Central Range, the Cantabrian Range and the Atlas Mountains. Blue arrows represent locations which may have undergone extensional deformation during the same period of time, identified from the strength of crustal anisotropy. In (a): AM: Atlas Mountains; CAR: Cantabrian Range; CR: Central Range; IC: Iberian Chain. In (b), two main regions with strong mantle anisotropy are highlighted.